

## Supporting information:

# A Conformational Role for NifW in the Maturation of Molybdenum Nitrogenase P-cluster

Casey Van Stappen<sup>a,†</sup>, Emilio Jiménez-Vicente<sup>b,†</sup>, Ana Pérez-González<sup>b</sup>, Zhi-Yong Yang<sup>c</sup>, Lance C. Seefeldt<sup>c</sup>, Serena DeBeer<sup>a</sup>, Dennis R. Dean<sup>b</sup>, Laure Decamps<sup>a\*</sup>

\*Correspondence to: [laure.decamps@cec.mpg.de](mailto:laure.decamps@cec.mpg.de)

### Table of Contents

Experimental Procedures .....	2
Supplementary Figures and Tables .....	4
References .....	12

## Experimental Procedures

**Protein Preparation:** Samples of  $\Delta^{HAZ}NifD_2K_2$  and  $\Delta^{HAZ}NifD_2K_2W_2$  were prepared from extracts of *Azotobacter vinelandii* strain DJ2122, containing in-frame deletions within both *nifH* and *nifZ* genes and carrying a sequence encoding a strep-tag placed at the N' terminus of NifD, allowing a one-step affinity purification.<sup>1</sup> The construction of DJ2122 and the corresponding residues respectively removed from NifH and NifZ, as well as the strep-tag sequence, have been previously described.<sup>2</sup> Construction of strain DJ2195 producing NifD<sub>2</sub>K<sub>2</sub> having the Cys275 residue substituted by Ala275 ( $C^{275A}NifD_2K_2$ ) and carrying a strep-tag located at the N' terminus of NifD was also previously described.<sup>2</sup>

*A. vinelandii* cells were grown in a 150-liter custom-built fermenter (W.B. Moore, Inc., Easton, PA) at 30°C in modified Burk medium containing 1  $\mu$ M Na<sub>2</sub>MoO<sub>4</sub> (J. T. Baker) as the Mo source and 5.7 mM ammonium acetate (Sigma) as the nitrogen source. After ammonium exhaustion, cells were derepressed for 4h and harvested. Strep-tagged  $\Delta^{HAZ}NifD_2K_2$  was purified following procedures previously described using Strep-Tactin columns (IBA Lifesciences, Göttingen, Germany).<sup>1</sup>

Further fractionation of  $\Delta^{HAZ}NifD_2K_2$  isolated by the one-step Strep-Tactin affinity procedure was performed by anion-exchange chromatography using buffers A (50 mM Tris pH 8.0, 2 mM sodium dithionite (DT)) and B (50 mM Tris pH 8.0, 500 mM NaCl, 2 mM DT) pH 8.0 as previously described. Further fractionation involved application of 77 mg of protein to a 5 mL Q-Sepharose column (Cytiva, Marlborough, MA) followed by elution using a 150 mM to 450 mM NaCl gradient (166 ml) using an AKTA purifier system (GE Healthcare) as previously described.<sup>3</sup> The fraction containing  $\Delta^{HAZ}NifD_2K_2$  eluted at 37 mS/cm and the fraction containing  $\Delta^{HAZ}NifD_2K_2W_2$  eluted at 49 mS/cm. Two other fractions contained either NafH or NifW, in sub-stoichiometric amounts, and were not further analyzed. Fractions collected were concentrated using 1mL Q-Sepharose columns (Cytiva, Marlborough, MA) for further characterization. Fractions were analyzed by SDS-PAGE (Figures 2 and S1), using a 4% acrylamide stacking gel and 15% acrylamide running gel followed by staining with Coomassie Brilliant Blue. The proteins indicated on Figures 2 and S1 were identified by mass spectrometry and molar ratios estimated by densitometry.<sup>3</sup> Purification of  $C^{275A}NifD_2K_2$  was performed as previously described.<sup>2</sup>

To characterize oxidized species, samples isolated in the DT-reduced state were desalted using an Illustra NAP-5 column (Cytiva, Marlborough, MA) equilibrated in buffer C (50 mM Tris pH 7.4, 200 mM NaCl), then incubated for 20' with a 10-fold excess of indigo disulfonate (IDS) before repeating the desalting step. Similarly, re-reduction (Figure S9) was performed by incubating oxidized samples with 5 mM DT, then desalting them in buffer C.<sup>4</sup>

**UV-vis measurements:** DT-reduced and IDS-oxidized protein samples were diluted in buffer C until reaching  $OD_{278} \approx 1$ . For each sample, 200  $\mu$ L were measured in a 1 mm-wide quartz cuvette using a DH-mini UV-Vis-NIR Deuterium-Halogen light source (Ocean Optics). Spectra were acquired with the Ocean View 2.0.8 software.

**X-ray Measurements:** X-ray absorption measurements were obtained at beamline 9-3 of the Stanford Synchrotron Radiation Lightsource (SSRL). The SPEAR storage ring operated at 3 GeV in top-off mode with a  $\sim$ 500 mA ring current. A liquid N<sub>2</sub>-cooled double-crystal monochromator with Si(220) crystals at  $\phi = 0^\circ$  was used to select the incoming X-ray energy with an intrinsic resolution ( $\Delta E/E$ ) of  $\sim 1.4 \times 10^{-4}$ , and a Rh-coated mirror was used for harmonic rejection at the Fe K-edge. The X-ray beam size was 1 x 5 mm<sup>2</sup> (v x h) at the sample position. Samples were maintained at cryogenic temperatures using a liquid He flow cryostat at SSRL ( $\sim$ 20 K) to minimize radiation damage and maintain an inert sample environment. Fluorescence measurements were recorded using a Canberra 100-element Ge monolith solid-state detector. Prior to measurements, each sample was checked for signs of radiation damage by performing subsequent 5-minute scans over the same sample spot. These tests showed all protein samples were stable under X-ray irradiation at the Fe K-edge for >40 minutes. All Fe XAS scans were collected by scanning the incident energy from 6882 to 8086 eV, and calibrated by simultaneous measurement of an Fe foil, with the first inflection point set to 7111.2 eV.

**X-ray data processing:** In all experiments, individual scans were normalized to the incident photon flux and energy calibrated using the program Athena from the software package Demeter. Further processing of spectra including background subtraction and scan averaging was also performed using Athena,<sup>5</sup> following standard protocols for X-ray spectroscopy.<sup>6-7</sup> Background subtraction and normalization were performed using a linear regression for the pre-edge region of 6968-7003 eV and a quadratic polynomial regression for the post-edge region of 7230-8000 eV. Data were splined from  $k = 0-16 \text{ \AA}^{-1}$  using an R-background of 1.0 and  $k$ -weight of 2.

**EXAFS data processing:** EXAFS fitting was performed using the program Artemis, also part of the software package Demeter. Possible scattering paths for the EXAFS models were initially determined using FEFF

6.0<sup>8</sup> in combination with crystal structures of reduced and oxidized NifD<sub>2</sub>K<sub>2</sub> (PDB ID: 3U7Q and 2MIN, respectively).<sup>9-10</sup> Due to the already considerable complexity of the EXAFS of NifD<sub>2</sub>K<sub>2</sub>, fitting was limited to include only single scattering paths. Previous studies have established that significant phase cancellation occurs among the Fe-Fe scatterers, and that the two distinct Fe-Fe scatterers needed to model this behavior.<sup>6, 11-12</sup> Therefore, based on these analyses a minimum of three single scattering paths were considered for all samples, specifically a single Fe-S and two distinct Fe-Fe scatterers referred to as Fe-Fe(1) and Fe-Fe(2). Additionally, based on previous observations for the crystal structures of oxidized NifD<sub>2</sub>K<sub>2</sub> (PDB ID: 2MIN, 5KOJ),<sup>9, 13</sup> the presence of a light atom scatterer was tested by addition of a fourth Fe-O scatterer. Importantly, Fe-O vs. Fe-N cannot be clearly distinguished to the similar scattering properties of O and N, and therefore this path is referred to as Fe-O/N. For all fits, the parameters  $R$  (bond distance),  $\sigma^2$  (bond variance), and  $E_0$  (ionization energy) were allowed to vary during fitting refinement. For each sample, a single value of  $\sigma^2$  was simultaneously fit for both Fe-Fe(1) and Fe-Fe(2) due to the similar nature of the scattering pathways and in an effort to reduce the number of free parameters. During refinement, values of  $N$  (degeneracy) were systematically varied by units of 0.125, which represents the minimum variation in coordination number that can occur for a system containing 8 unique absorbers of the same identity. For the unknown structures  $\Delta_{\text{HAZ}}\text{NifD}_2\text{K}_2$  and  $\Delta_{\text{HAZ}}\text{NifD}_2\text{K}_2\text{W}_2$ , the total Fe-Fe coordination number [Fe-Fe(1) + Fe-Fe(2)] was fixed to 3, and the relative ratio of Fe-Fe(1):Fe-Fe(2) was varied. Meanwhile, total coordination numbers for Fe-Fe in the reduced and oxidized forms of  $^{275}\text{A}\text{NifD}_2\text{K}_2$  were based on available crystal structures of the mature P-cluster, which support  $N = 3.5$  in the reduced form and  $N < 3$  in the IDS oxidized form.<sup>9-10, 13</sup> A fixed value of  $S_0^2 = 0.9$  was used in all EXAFS fits. A  $k$ -range of 3-13 Å<sup>-1</sup> was used in the curve fitting analysis of all spectra, providing a maximum resolution of  $\Delta R = 0.157$  Å and 12.4 degrees of freedom. All data were fit in  $R$ -space using an  $R$ -range of 1.0 to 3.0 Å.

**EPR Measurements:** Continuous wave (CW) electron paramagnetic resonance (EPR) measurements were performed at X-band frequency (~9.65 GHz) using a Bruker E500 ELEXSYS spectrometer equipped with a Bruker dual-mode cavity (ER4116DM) and an Oxford Instruments helium-flow cryostat (ESR 900). A high-sensitivity Bruker Super-X (ER-049X) bridge with an integrated microwave frequency counter was employed, along with a magnetic field controller (ER032T) that was calibrated using a Bruker NMR field probe (ER035M). All measurements utilized a 7.46 G modulation amplitude with a 100 kHz modulation frequency, and an 80.92 ms time constant. For temperature dependent measurements, 1 mW microwave power was used. All spectra were recorded on frozen solutions. All spectra were processed and analyzed using the software package *EasySpin* (version 5.2.30), as implemented in *Matlab* (version R2018b). Spin quantification was calculated from the Asaa-Vanngard corrected doubly integrated spectral intensities of the baseline-corrected, background subtracted spectra relative to a CuSO<sub>4</sub>•5H<sub>2</sub>O spin standard.<sup>14</sup>

## Supplementary Figures and Tables

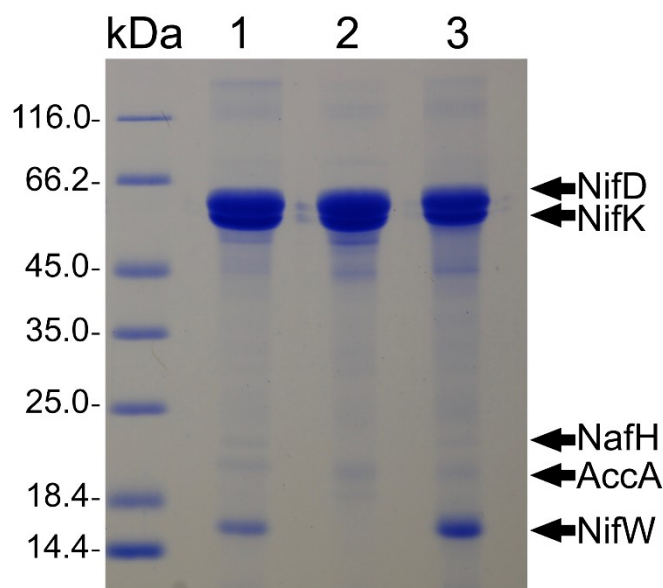


**Figure S1.** SDS-PAGE analysis of the same protein samples as shown in Figure 2, but with more sample loaded per lane. This analysis reveals the presence of NafH in lanes 1 and 3, as well as the acetate carboxylase AccA subunit. The latter co-purified nonspecifically during Strep-tactin affinity purification because acetate carboxylase is a biotin-binding protein. The  $\Delta^{HAZ}NifD_2K_2NafH_x$  species represents less than 8% of the total sample. Bands other than those labelled are fragments of hydrolyzed NifD and NifK.

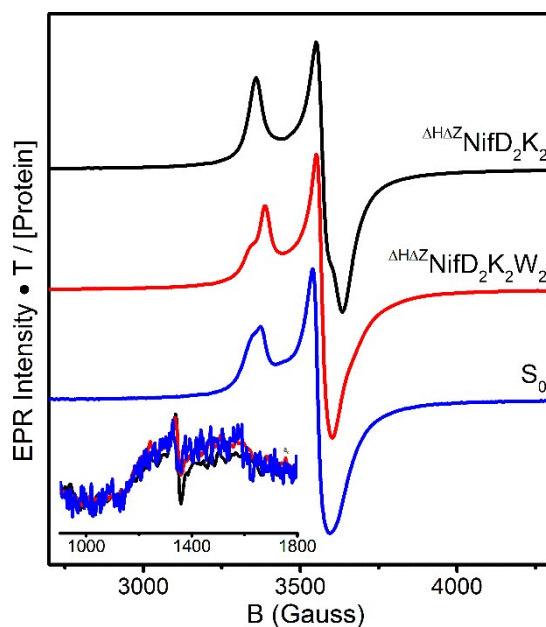


**Figure S2.** Comparison of perpendicular mode X-band EPR spectra of DT-reduced  $\Delta^{HAZ}NifD_2K_2$  (black),  $\Delta^{HAZ}NifD_2K_2W_2$  (red), and proteins isolated by one-step Strep-tag affinity purification ( $S_0$ , blue). These spectra correspond to samples isolated in lanes 2, 3, and 1, respectively, of figures 2 and S1. Spectra were measured at 14 K, 1 mW, and 9.65 GHz.

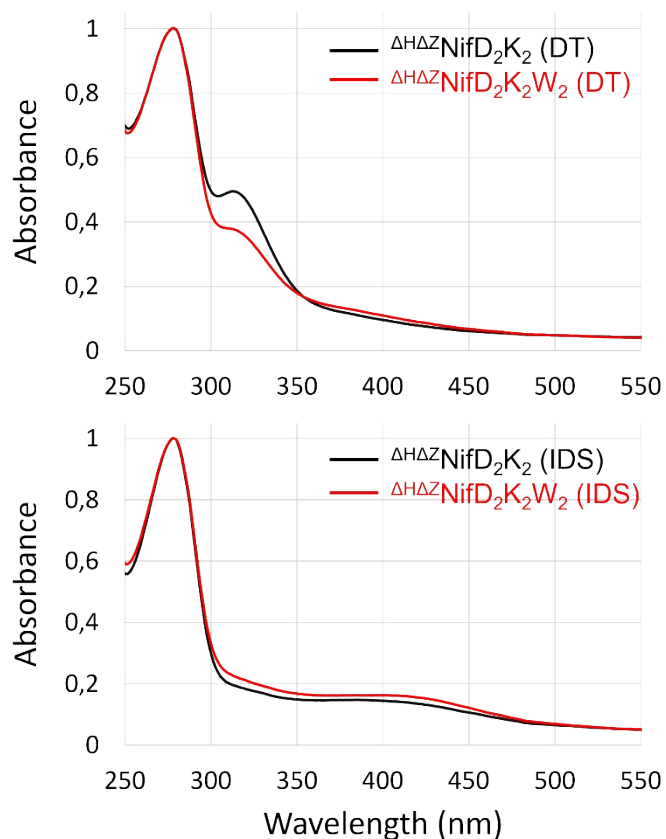


**Figure S3.** UV-vis spectra of the  $\Delta^{\text{HAZ}}\text{NifD}_2\text{K}_2(\text{W}_2)$  species after DT-reduction (top) or IDS-oxidation (bottom). Spectra were acquired on samples with a protein concentration of  $\sim 10$  mg/ml and normalized to  $\text{OD}_{278} = 1$ .

Besides the peak at 315 nm originating from sodium dithionite, the spectrum of DT-reduced  $\Delta^{\text{HAZ}}\text{NifD}_2\text{K}_2$  appeared featureless, while the spectrum of DT-reduced  $\Delta^{\text{HAZ}}\text{NifD}_2\text{K}_2\text{W}_2$  displayed a low inflection with a maximum at 380 nm. No signal around 500 nm could be observed in the UV-vis spectra of reduced samples, consistent with the expected lack of mature P-cluster.<sup>2, 15-16</sup> Upon IDS reduction, the spectra of both samples displayed features typical of oxidized iron-sulfur clusters, with shoulders around 320 nm and 420 nm. Similar features had previously been reported for  $\Delta^{\text{H}}\text{NifD}_2\text{K}_2$ .<sup>2</sup> Interestingly, the shoulders of IDS-oxidized  $\Delta^{\text{HAZ}}\text{NifD}_2\text{K}_2\text{W}_2$  appear to display a slight redshift compared to IDS-oxidized  $\Delta^{\text{HAZ}}\text{NifD}_2\text{K}_2$ .

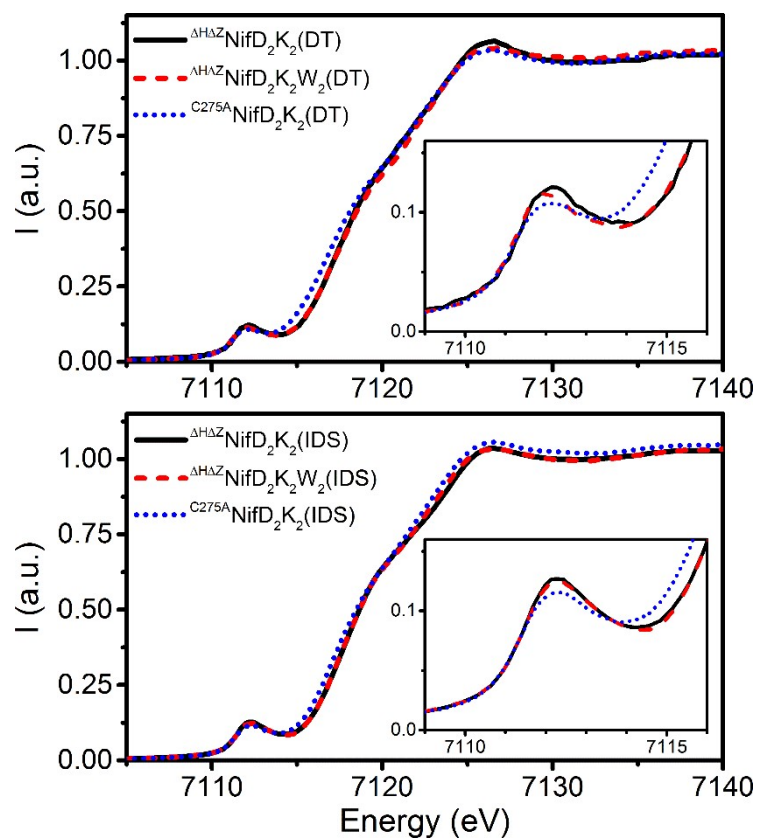


**Figure S4.** Comparison of the normalized Fe K-edge XAS spectra of  $\Delta\text{HAZNiF}_2\text{K}_2$  (black),  $\Delta\text{HAZNiF}_2\text{K}_2\text{W}_2$  (red), and  $\text{C}^{275\text{A}}\text{NiF}_2\text{K}_2$  (blue) in the DT-reduced (top) and IDS-oxidized (bottom) forms. Insets show an expanded view of the pre-edge region from 7109-7116 eV.

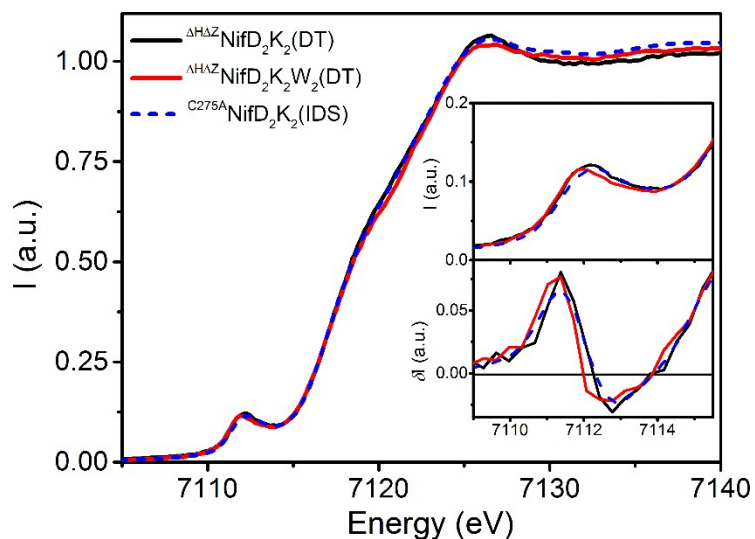


**Figure S5.** Fe K-edge XAS of  $\Delta\text{HAZNiF}_2\text{K}_2(\text{DT})$  (black, solid),  $\Delta\text{HAZNiF}_2\text{K}_2\text{W}_2(\text{DT})$  (red, solid), and  $\text{C}^{275\text{A}}\text{NiF}_2\text{K}_2(\text{IDS})$  (blue, dashed). The top inset provides an expanded view of the pre-edge region, and the bottom inset provides the equivalent first derivative spectra. The rising edge position from 7114-7118 eV appear near identical. Small modulations are observed in the pre-edge region, where  $\Delta\text{HAZNiF}_2\text{K}_2(\text{DT})$  appears more intense and  $\Delta\text{HAZNiF}_2\text{K}_2\text{W}_2(\text{DT})$  shifted down in energetic position relative to  $\text{C}^{275\text{A}}\text{NiF}_2\text{K}_2(\text{IDS})$ .

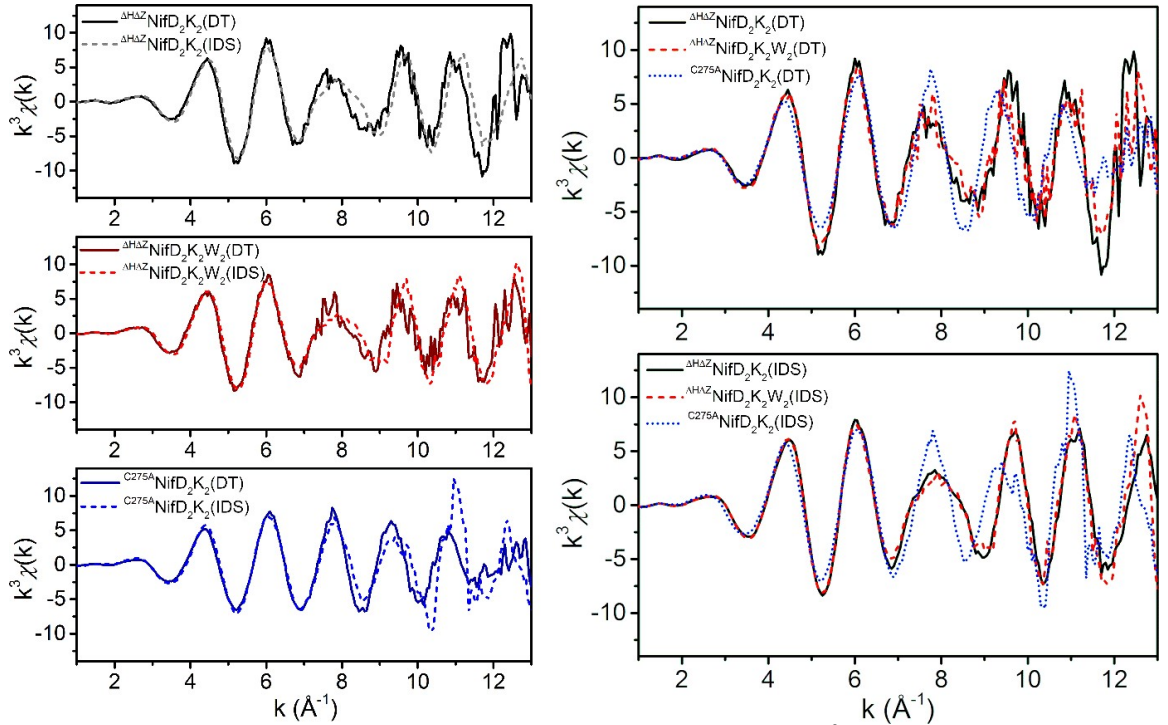


**Figure S6.** Comparison of the Fe EXAFS of the presently studied variants in  $k^3$ -space. Left, One-to-one comparisons of the DT-reduced (solid) and IDS-oxidized (dashed) forms of  $\Delta^{\text{HAZ}}\text{NiFD}_2\text{K}_2$  (top),  $\Delta^{\text{HAZ}}\text{NiFD}_2\text{K}_2\text{W}_2$  (middle), and  $\text{C}^{275\text{A}}\text{NiFD}_2\text{K}_2$  (bottom). Right, Comparison of the DT-reduced (top) and IDS-oxidized (bottom) forms.

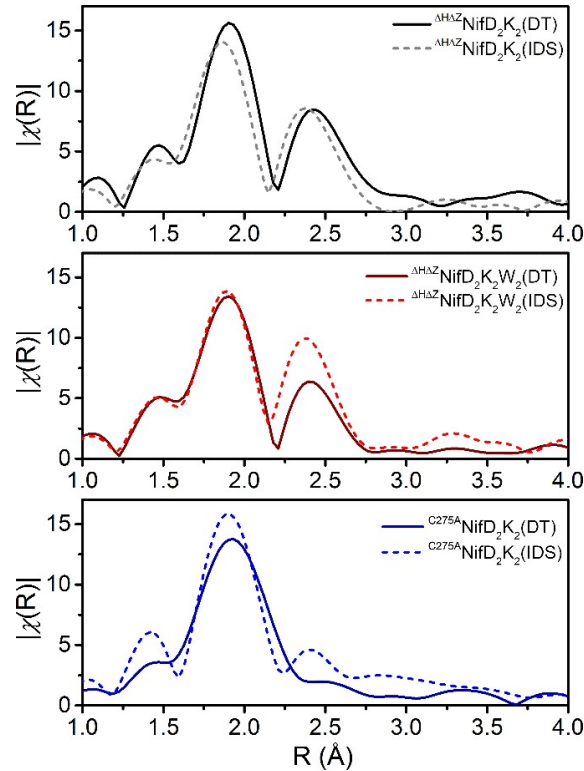


**Figure S7.** One-to-one Fe EXAFS comparisons in R-space of the DT-reduced (solid) and IDS-oxidized (dashed) forms of  $\Delta^{\text{HAZ}}\text{NiFD}_2\text{K}_2$  (top),  $\Delta^{\text{HAZ}}\text{NiFD}_2\text{K}_2\text{W}_2$  (middle), and  $\text{C}^{275\text{A}}\text{NiFD}_2\text{K}_2$  (bottom). Spectra were produced using  $k^3$ -weighting, and a  $k$ -range of 3-13  $\text{\AA}^{-1}$ .

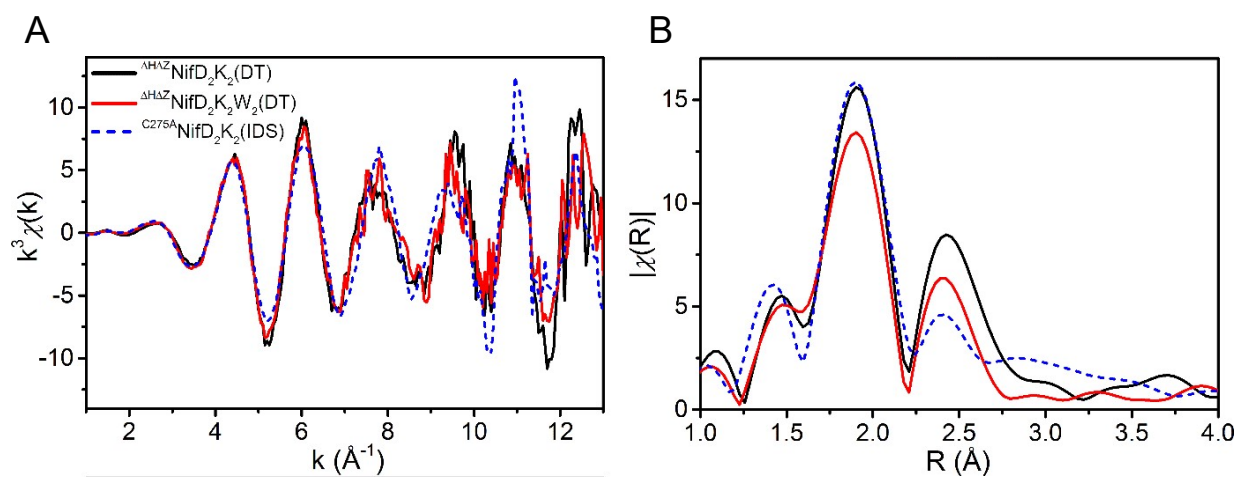


**Figure S8.** Fe EXAFS of  $\Delta\text{HAZNiF}_2\text{K}_2(\text{DT})$  (black, solid),  $\Delta\text{HAZNiF}_2\text{K}_2\text{W}_2(\text{DT})$  (red, solid), and  $\text{C}^{275\text{A}}\text{NiF}_2\text{K}_2(\text{IDS})$  (blue, dashed) in both  $k^3$ -space (A) and R-space (B). The Fourier transform spectra were produced using  $k^3$ -weighting, and a  $k$ -range of 3-13  $\text{\AA}^{-1}$ .

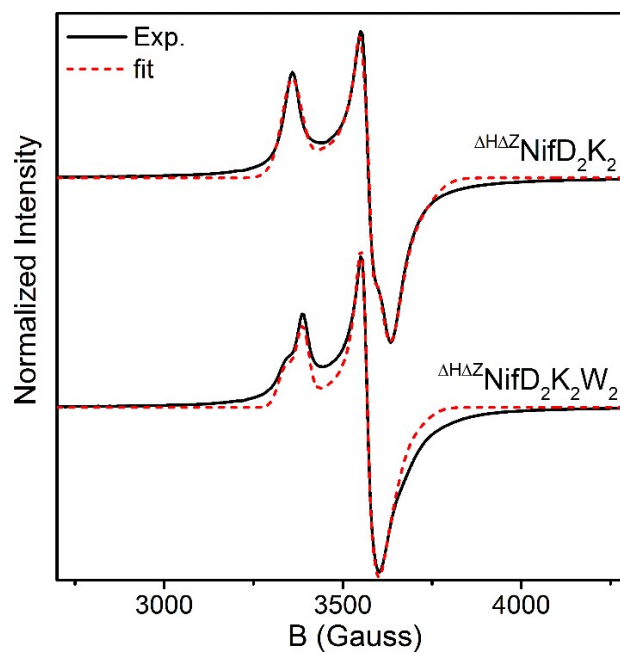


**Figure S9.** Fitting of X-band EPR spectra of DT-reduced  $\Delta\text{HAZNiF}_2\text{K}_2$  (top) and  $\Delta\text{HAZNiF}_2\text{K}_2\text{W}_2$  (bottom) at 14 K.

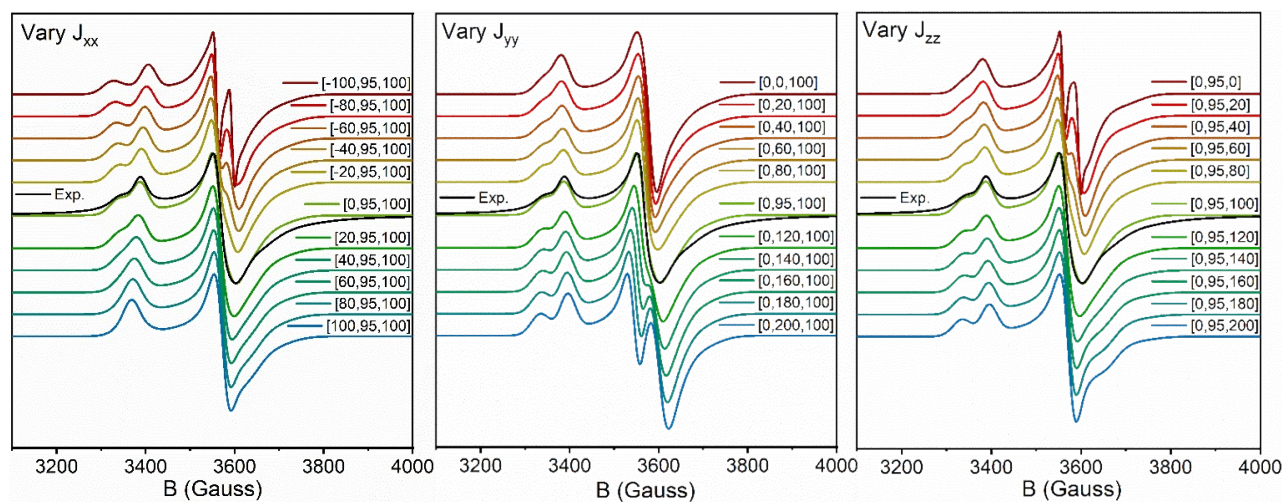


**Figure S10.** Dependence of simulated spectra on  $\Delta\text{HAZNiF}_2\text{K}_2\text{W}_2$  on the principal values of the diagonalized electron-electron interaction matrix  $[J_{xx}, J_{yy}, J_{zz}]$ , provided in MHz. The experimental X-band EPR spectrum at 14 K (black) is provided for comparison.

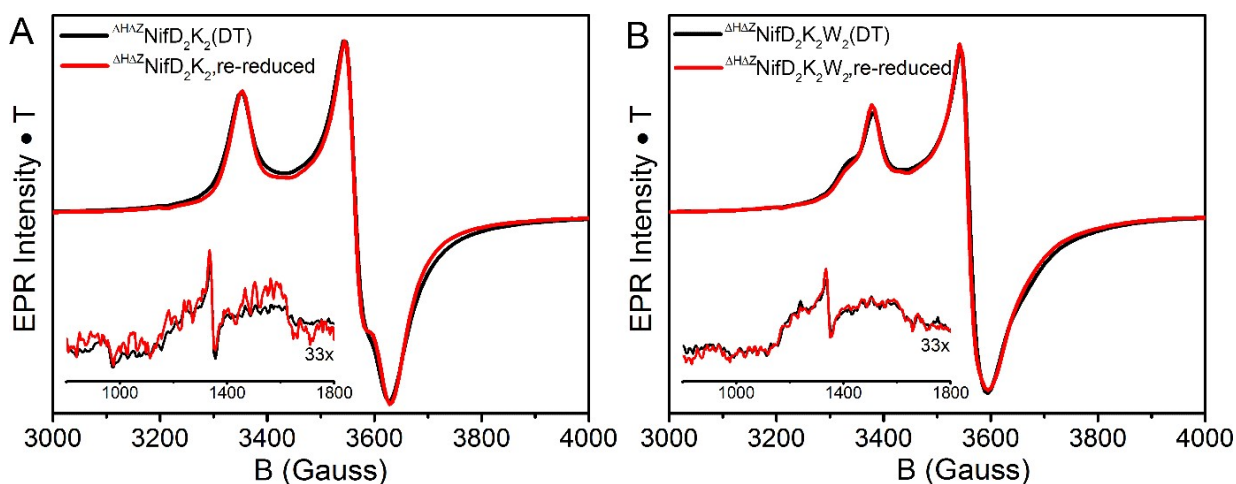


**Figure S11.** X-band EPR spectra of A)  $\Delta^{\text{HAZ}}\text{NiD}_2\text{K}_2$  and B)  $\Delta^{\text{HAZ}}\text{NiD}_2\text{K}_2\text{W}_2$  in the presence of sodium dithionite (black), and after IDS oxidation and desalting followed by re-reduction with sodium dithionite. All spectra are normalized for temperature, power, collection time, and gain. Spectra were measured at 14 K, 1 mW, and 9.65 GHz. In both complexes, spectra look identical in reduced and re-reduced samples, showing that the observed signals do not originate from oxidation-induced cluster damage and that the IDS oxidation of the clusters in the  $\Delta^{\text{HAZ}}\text{NiD}_2\text{K}_2$  and  $\Delta^{\text{HAZ}}\text{NiD}_2\text{K}_2\text{W}_2$  samples is a reversible process.

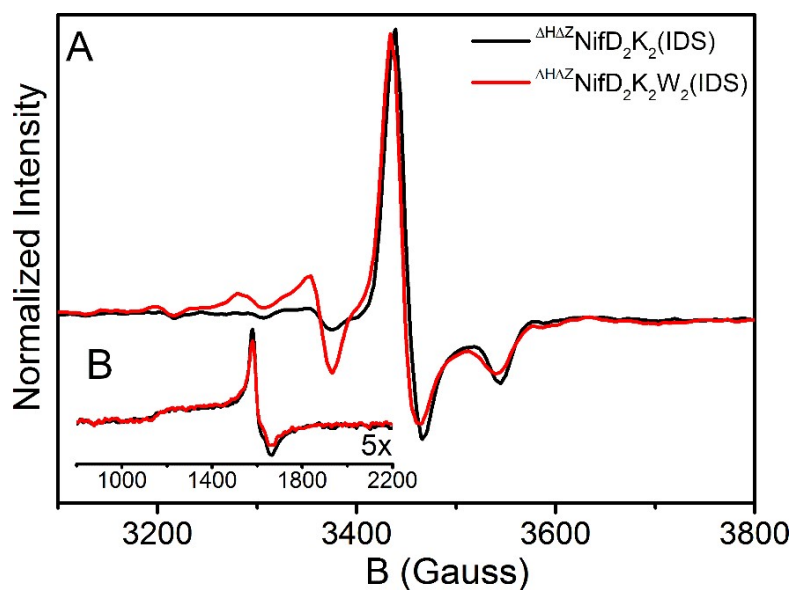


**Figure S12.** Comparison of IDS-oxidized  $\Delta^{\text{HAZ}}\text{NiD}_2\text{K}_2$  (black) and  $\Delta^{\text{HAZ}}\text{NiD}_2\text{K}_2\text{W}_2$  (red) over A) the intermediate-field region at 50 K, and B) the low-field region at 5 K.

**Table S1.** Summary of EXAFS fitting results for reduced and oxidized  $\Delta\text{H}\Delta\text{Z}\text{NiF}_2\text{K}_2$ ,  $\Delta\text{H}\Delta\text{Z}\text{NiF}_2\text{K}_2\text{W}_2$ , and  $\text{C}^{275\text{A}}\text{NiF}_2\text{K}_2$ , with and without a light atom scatterer. Values of  $\sigma^2$  are in units of  $10^{-3} \text{ \AA}^2$ , and distances R are in unit of  $\text{\AA}$ . Fits were performed for a k-range of  $3\text{-}13 \text{ \AA}^{-1}$  and  $R = 1\text{-}3 \text{ \AA}$ .

Sample	Fe-S			Fe-Fe(1)			Fe-Fe(2)			Fe-O/N			$E_0$ (eV)	Error		
	N	R	$\sigma^2$	N	R	$\sigma^{2a}$	N	R	$\sigma^{2a}$	N	R	$\sigma^2$		$\chi^2$	Red. $\chi^2$	R-factor
$\Delta\text{H}\Delta\text{Z}\text{NiF}_2\text{K}_2$ (DT)	3.5	2.30 (0.01)	3.7 (0.4)	0.75	2.53 (0.02)	3.4 (0.6)	2.25	2.72 (0.01)	3.4	---	---	---	7119.4 (1)	35	6.4	0.0081
	3.5	2.31 (0.01)	4.0 (0.5)	0.75	2.51 (0.03)	3.6 (0.8)	2.25	2.73 (0.01)	3.6	0.5	2.08 (0.09)	6.0 (0.1)	7120.5 (1)	31	8.9	0.0072
$\Delta\text{H}\Delta\text{Z}\text{NiF}_2\text{K}_2$ (IDS)	3	2.27 (0.01)	3.1 (0.4)	0.5	2.47 (0.05)	5.5 (0.9)	2.5	2.70 (0.01)	5.5	---	---	---	7117.1 (1)	529	82	0.0121
	3	2.28 (0.01)	2.9 (0.1)	0.5	2.44 (0.05)	6.0 (0.8)	2.5	2.70 (0.01)	6.0	0.25	2.05 (0.01)	4.1 (0.2)	7118.3 (2)	501	146	0.0115
$\Delta\text{H}\Delta\text{Z}\text{NiF}_2\text{K}_2\text{W}_2$ (DT)	3.25	2.30 (0.01)	3.9 (0.6)	0.75	2.49 (0.05)	6.2 (1.5)	2.25	2.71 (0.01)	6.2	---	---	---	7117.7 (2)	60	9.3	0.0214
	3.25	2.30 (0.02)	3.5 (1.1)	0.75	2.47 (0.04)	6.5 (2.1)	2.25	2.71 (0.01)	6.5	0.5	1.97 (0.06)	1.5 (0.3)	7117.3 (3)	40	8.5	0.0141
$\Delta\text{H}\Delta\text{Z}\text{NiF}_2\text{K}_2\text{W}_2$ (IDS)	3	2.28 (0.01)	3.1 (0.4)	0.5	2.47 (0.03)	4.6 (0.7)	2.5	2.71 (0.01)	4.6	---	---	---	7118.0 (1)	348	54	0.0163
	3	2.28 (0.01)	3.0 (2.9)	0.5	2.47 (0.01)	4.6 (0.5)	2.5	2.70 (0.01)	4.6	0.5	1.93 (0.03)	1.3 (0.2)	7117.6 (1)	236	53	0.0113
$\text{C}^{275\text{A}}\text{NiF}_2\text{K}_2$ (DT)	3	2.29 (0.01)	3.5 (0.3)	2	2.57 (0.01)	6.9 (0.7)	1.5	2.80 (0.01)	6.3	---	---	---	7115.0 (1)	61	11.2	0.0043
	3	2.29 (0.01)	3.5 (0.4)	2	2.56 (0.01)	6.8 (0.9)	1.5	2.80 (0.01)	6.3	0.13	1.90 (0.09)	1.0 (0.3)	7114.6 (1)	55	15.9	0.0039
$\text{C}^{275\text{A}}\text{NiF}_2\text{K}_2$ (IDS)	3.25	2.29 (0.02)	4.2 (1.0)	1	2.50 (0.02)	2.2 (1.9)	1.25	2.70 (0.01)	2.2	---	---	---	7116.0 (3)	327	60	0.0406
	3.25	2.28 (0.02)	4.2 (1.1)	1	2.50 (0.02)	1.8 (2.2)	1.25	2.70 (0.02)	1.8	0.25	1.87 (0.11)	1.5 (0.5)	7114.8 (3)	311	90	0.0386

<sup>a</sup> A single  $\sigma^2$  was simultaneously fit for both Fe-Fe(1) and Fe-Fe(2) paths.

**Table S2.** Summary of EPR fitting parameters for  $\Delta\text{H}\Delta\text{Z}\text{NiF}_2\text{K}_2$  (DT) and  $\Delta\text{H}\Delta\text{Z}\text{NiF}_2\text{K}_2\text{W}_2$  (DT). Fits for  $\Delta\text{H}\Delta\text{Z}\text{NiF}_2\text{K}_2$  (DT) are included for both with and without the inclusion of an e-e interaction.

Sample	$[g_1, g_2, g_3]$		gStrain		e-e interaction (MHz) [ $J_{xx}, J_{yy}, J_{zz}$ ]
	Component 1	Component 2	Component 1	Component 2	
$\Delta\text{H}\Delta\text{Z}\text{NiF}_2\text{K}_2$ (DT)	[2.0591, 1.9355, 1.8461]	[2.0590, 1.9172, 1.9094]	[0.0248, 0.0136, 0.0815]	[0.0802, 0.0396, 0.0549]	---
$\Delta\text{H}\Delta\text{Z}\text{NiF}_2\text{K}_2$ (DT)	[2.0603, 1.9357, 1.8511]	[2.0596, 1.9194, 1.9071]	[0.0228, 0.0140, 0.0742]	[0.0780, 0.0418, 0.0507]	[-16, 35, -37]
$\Delta\text{H}\Delta\text{Z}\text{NiF}_2\text{K}_2\text{W}_2$ (DT)	[2.0583, 1.9307, 1.8697]	[2.0394, 1.9270, 1.9040]	[0.0329, 0.0233, 0.0496]	[0.0216, 0.0050, 0.0350]	[0, 95, 100]

## References

1. Jimenez-Vicente, E.; Martin Del Campo, J. S.; Yang, Z. Y.; Cash, V. L.; Dean, D. R.; Seefeldt, L. C., Application of affinity purification methods for analysis of the nitrogenase system from *Azotobacter vinelandii*. *Methods Enzymol* **2018**, *613*, 231-255.
2. Jimenez-Vicente, E.; Yang, Z. Y.; Ray, W. K.; Echavarri-Erasun, C.; Cash, V. L.; Rubio, L. M.; Seefeldt, L. C.; Dean, D. R., Sequential and differential interaction of assembly factors during nitrogenase MoFe protein maturation. *J Biol Chem* **2018**, *293* (25), 9812-9823.
3. Jimenez-Vicente, E.; Yang, Z. Y.; Martin Del Campo, J. S.; Cash, V. L.; Seefeldt, L. C.; Dean, D. R., The NifZ accessory protein has an equivalent function in maturation of both nitrogenase MoFe protein P-clusters. *J Biol Chem* **2019**, *294* (16), 6204-6213.
4. Christiansen, J.; Goodwin, P. J.; Lanzilotta, W. N.; Seefeldt, L. C.; Dean, D. R., Catalytic and biophysical properties of a nitrogenase Apo-MoFe protein produced by a nifB-deletion mutant of *Azotobacter vinelandii*. *Biochemistry-Us* **1998**, *37* (36), 12611-23.
5. Ravel, B.; Newville, M., ATHENA, ARTEMIS, HEPHAESTUS: data analysis for X-ray absorption spectroscopy using IFEFFIT. *J Synchrotron Radiat* **2005**, *12* (Pt 4), 537-41.
6. Van Stappen, C.; Thorhallsson, A. T.; Decamps, L.; Bjornsson, R.; DeBeer, S., Resolving the structure of the E1 state of Mo nitrogenase through Mo and Fe K-edge EXAFS and QM/MM calculations. *Chemical Science* **2019**, *10* (42), 9807-9821.
7. Cutsail, G. E., 3rd; Banerjee, R.; Zhou, A.; Que, L., Jr.; Lipscomb, J. D.; DeBeer, S., High-Resolution Extended X-ray Absorption Fine Structure Analysis Provides Evidence for a Longer Fe...Fe Distance in the Q Intermediate of Methane Monooxygenase. *J Am Chem Soc* **2018**, *140* (48), 16807-16820.
8. Zabinsky, S. I.; Rehr, J. J.; Ankudinov, A.; Albers, R. C.; Eller, M. J., Multiple-scattering calculations of x-ray-absorption spectra. *Phys Rev B Condens Matter* **1995**, *52* (4), 2995-3009.
9. Peters, J. W.; Stowell, M. H.; Soltis, S. M.; Finnegan, M. G.; Johnson, M. K.; Rees, D. C., Redox-dependent structural changes in the nitrogenase P-cluster. *Biochemistry-Us* **1997**, *36* (6), 1181-7.
10. Spatzal, T.; Aksoyoglu, M.; Zhang, L.; Andrade, S. L.; Schleicher, E.; Weber, S.; Rees, D. C.; Einsle, O., Evidence for interstitial carbon in nitrogenase FeMo cofactor. *Science* **2011**, *334* (6058), 940.
11. Christiansen, J.; Tittsworth, R. C.; Hales, B. J.; Cramer, S. P., Fe and Mo EXAFS of *Azotobacter vinelandii* Nitrogenase in Partially Oxidized and Singly Reduced Forms. *J Am Chem Soc* **1995**, *117* (40), 10017-10024.
12. Musgrave, K. B.; Liu, H. I.; Ma, L.; Burgess, B. K.; Watt, G.; Hedman, B.; Hodgson, K. O., EXAFS studies on the PN and POX states of the P-clusters in nitrogenase. *JBIC Journal of Biological Inorganic Chemistry* **1998**, *3* (4), 344-352.
13. Rutledge, H. L.; Rittle, J.; Williamson, L. M.; Xu, W. A.; Gagnon, D. M.; Tezcan, F. A., Redox-Dependent Metastability of the Nitrogenase P-Cluster. *J Am Chem Soc* **2019**, *141* (25), 10091-10098.
14. Aasa, R.; Vanngard, T., Epr Signal Intensity and Powder Shapes - Re-Examination. *J Magn Reson* **1975**, *19* (3), 308-315.
15. Ribbe, M. W.; Hu, Y.; Guo, M.; Schmid, B.; Burgess, B. K., The FeMoco-deficient MoFe protein produced by a nifH deletion strain of *Azotobacter vinelandii* shows unusual P-cluster features. *J Biol Chem* **2002**, *277* (26), 23469-76.
16. Hu, Y.; Corbett, M. C.; Fay, A. W.; Webber, J. A.; Hedman, B.; Hodgson, K. O.; Ribbe, M. W., Nitrogenase reactivity with P-cluster variants. *Proc Natl Acad Sci U S A* **2005**, *102* (39), 13825-30.